AGU ADVANCING EARTH AND SPACE SCIENCE

Geophysical Research Letters

RESEARCH LETTER

10.1029/2022GL098043

Key Points:

- We recreate the generation of tidal vortices at different scales around tidal inlets using a laboratory model
- Vortices shed around the inlet undergo a merging-thinning process leading to macro flow gyres that occupy the entire tidal flats
- The results of filter-space analysis demonstrate the coexistence of energy and enstrophy multiple cascades depending on the tidal phase

Supporting Information:

Supporting Information may be found in the online version of this article.

Correspondence to:

A. Stocchino,
alessandro.stocchino@polyu.edu.hk

Citation:

De Leo, A., & Stocchino, A. (2022). Evidence of transient energy and enstrophy cascades in tidal flows: A scale to scale analysis. *Geophysical Research Letters*, *49*, e2022GL098043. https://doi.org/10.1029/2022GL098043

Received 27 JAN 2022
Accepted 11 MAY 2022

Author Contributions:

Conceptualization: A. De Leo, A. Stocchino
Formal analysis: A. De Leo
Investigation: A. Stocchino
Methodology: A. De Leo, A. Stocchino
Software: A. De Leo
Visualization: A. De Leo
Writing – original draft: A. Stocchino
Writing – review & editing: A. De Leo

Evidence of Transient Energy and Enstrophy Cascades in Tidal Flows: A Scale to Scale Analysis

A. De Leo[1] and A. Stocchino[2,3]

[1]Dipartimento di Ingegneria Civile, Chimica e Ambientale, Università degli Studi di Genova, Genova, Italia, [2]Department of Civil and Environmental Engineering, Hong Kong Polytechnic University, Kowloon, Hong Kong, [3]State Key Laboratory of Marine Pollution, City University of Hong Kong, Kowloon, Hong Kong

Abstract Tidal currents are predominant in coastal areas, causing the generation of vortices at different scales. We reproduce the main process of vortex shedding generated in tidal systems with inlets and channels using a laboratory large-scale model. A filter-space technique is implemented to analyze nonlinear energy/enstrophy transfer rates and map out the energy pathways through the flow scales of the measured velocity fields. We provide sound evidence of the transitional character of the energy cascades during a tidal period. The periodic generation and destruction of tidal vortices plays a relevant role in the transition from an inverse to a direct energy cascade within a tidal period. The period-averaged energy budget shows the coexistence of multiple cascades. Small scales follow a direct energy cascade, whereas a split-energy cascade is found at intermediate and large scales, where part of the injected energy goes to small scales and part to a larger flow scale.

Plain Language Summary Remote sensing images from a satellite of ocean and coastal areas offer unique opportunities to observe vortical flow structures. Coastal areas are often dominated by tidal currents that interact with coastline features (island, headlands or capes, and inlets) and periodically shed vortices at different scales. Coastal vortices are known to play a fundamental role in momentum, mass, and energy transport. Understanding how energy is exchanged among the wide range of flow scales (small/large vortices and large-scale tidal circulations) is a fundamental question that deserves a thorough investigation, owing to the great impact on the coastal dynamics. With this in mind, we used a large-scale physical model to accurately recreate the main processes that lead to the generation of tidal vortices observed around natural inlets. The measured velocity fields have been analyzed with filtering techniques that allow for understanding the direction of energy exchanges. We demonstrated that the periodicity of the tidal flow produces multiple energy cascades depending on the tidal phase. We found that energy followed dual pathways toward large scales and vice versa.

1. Introduction

Understanding how energy travels through a turbulent system, both spatially and with respect to flow scales, has been historically challenging. The seminal paper of Kolmogorov (1941), who provided the first description of the energy cascade in a self-similar fashion, has inspired the research in high Reynolds number flows for decades. Since then, the celebrated $-5/3$ power law in the inertial range has been challenged especially for two dimensional or quasi-two dimensional turbulent flows, see Alexakis and Biferale (2018) for a comprehensive review on energy cascades. Flow inhomogeneities, such as coherent vortices, and two dimensionality proved to force different scaling and, in some cases, more than a power law appears, depending on the range of wavenumbers considered. Coherent structures are indeed able to control the overall energy transfers (Thiesset & Danaila, 2020).

Geophysical flows are extraordinary examples where the energy can be exchanged among the different flow scales following both direct cascades (from large scales to small scales as in the classical Kolmogorov view) and inverse pathways, that is, small flow scales transfer energy to mean flow, or even multiple cascades. Several examples of estimates of energy budget and fluxes in the ocean can be found in the literature and most of them deal with open ocean domains (Aluie et al., 2018; Khatri et al., 2018; Poje et al., 2017; Savage et al., 2017; Scott & Wang, 2005; Torres et al., 2018).

Tidal energy pathways and the associated tidal energy cascade is important owing to its influence on the ocean energy budget and climate (Kelly et al., 2012). Tides can generate high energy currents that, interacting with coastal features such as headlands, capes, and tidal inlets, trigger the formation of tidal vortices in a wide range of scales. Coastal tidal vortices tend to be quasi-2D vortical structures with horizontal dimensions typically much larger than the flow depth. Their importance in momentum, mass, and energy transport is well recognized (Blondeaux & Vittori, 2020; Enrile et al., 2018, 2019; Geyer & MacCready, 2014; MacCready & Geyer, 2010; Nicolau del Roure et al., 2009; Suara et al., 2017; Whilden et al., 2014). Remote sensing observations from a satellite or high-frequency coastal radars helped to identify this complex dynamics. An example is reported in Figure 1 where macrovortices generated by tidal currents in the western Sea of Okhotsk around the Shantar Islands and Uda Bay have been recently captured by Landsat 8. This image is an outstanding example of the variety of vortices at different scales that can be generated during high tides. In fact, intense tidal currents interacting with the coastline shed vortices in the form of von Karman streets with the typical horizontal scale in a range between 500 and 800 m over a mean depth of 30 m, which ultimately contribute to the generation of larger vortices (Zhabin & Luk'yanova, 2020).

In the context of geophysical flows, the study of energy cascades commonly relies on standard methods based on Fourier analysis (Khatri et al., 2018; Scott & Wang, 2005; Siegelman et al., 2022). Fourier spectral analysis provided important results but limited in their applicability to quasi-homogeneous regions with simple boundary conditions, and the techniques typically require some kind of special treatment at the boundaries. Few studies, instead, introduced the use of filter-space technique (FST) (Aluie et al., 2018), widely and successfully used in turbulent flow analysis (Aluie, 2011; Aluie & Eyink, 2009, 2010; Aluie & Kurien, 2011; Chen et al., 2003; Eyink, 1995; Eyink & Aluie, 2009; Germano, 1992; Liao & Ouellette, 2013, 2014; Liu et al., 1994). Different from Fourier spectral analysis, FST retains the spatial distribution of the fluxes and their direction, thus, clearly indicating whether the process exhibits a direct or inverse energy/enstrophy cascade. Moreover, FST helps in avoiding spurious effects that might arise by applying FFT on finite and non-periodic domains, as discussed in (Aluie et al., 2018).

The present study has the specific purpose to understand the energy and enstrophy transfers caused by the periodic generation and destruction of coherent vortices induced by a tidal flow. To this end, we designed a series of experiments using a large-scale flume with the aim to reproduce a tidal flow in a domain that resembles a tidal channel with lateral flats, communicating with the open ocean through a tidal inlet. The dimensions of the tidal flume allow for the development of a sufficiently high Reynolds number flow and the generation of a wide range of turbulent flow scales, similar to the vortices shown in the satellite image of Figure 1. The measured velocity fields have been analyzed using FST to accurately compute the spectral fluxes among the flow scales and within a tidal period, possibly leading to a better understanding of the tidal energy pathways and cascades.

2. Material and Methods

2.1. Experimental Setup and Measuring Techniques

The experiments have been carried out in a large scale tidal flume composed of two main parts: a basin and a tidal compound channel with exponentially decreasing width landward, divided by a tidal inlet. A sketch of the experimental setup is shown in Figure S1 in Supporting Information S1 together with the details of the apparatus and the particle image velocimetry (PIV) equipment used. The tidal inlet geometry mimic a so-called *barrier island* following the classification of previous studies (Nicolau del Roure et al., 2009; Valle-Levinson, 2010; Vouriot et al., 2019). Different tidal waves have been tested varying the tidal period T and amplitude a, with the assumption of small amplitude waves $\epsilon = a/D_0 \ll 1$, where D_0 is the mean water depth, set at 0.12 m. Thus, the corresponding inviscid wavelength is estimated as $L_g = T\sqrt{gD_0}$ (Cai et al., 2012; Toffolon et al., 2006).

A particular attention will be dedicated to the processes during the different tidal phase, that is, flood, when the mean flow is directed toward the channel, and ebb, when the mean flow reveres and is directed toward the basin (open sea).

The present experiments have been designed imposing a similitude based on the external dimensionless parameters suggested by Toffolon et al. (2006), namely the convergence ratio parameter ($\gamma = L_g/(2\pi L_b)$, where L_b is the convergence length) and the friction parameter ($\chi = \epsilon L_g/(2\pi C^2 D_0)$, where C is the Chézy coefficient) that represents the ratio between friction and inertia. For the present study, we imposed similitude laws preserving the friction parameter, see Supporting Information S1 for the details. Based on our parameters reported in Table S1 in Supporting Information S1, the experiments well represent weakly convergent and weakly dissipative estuarine environments as classified in Toffolon et al. (2006).

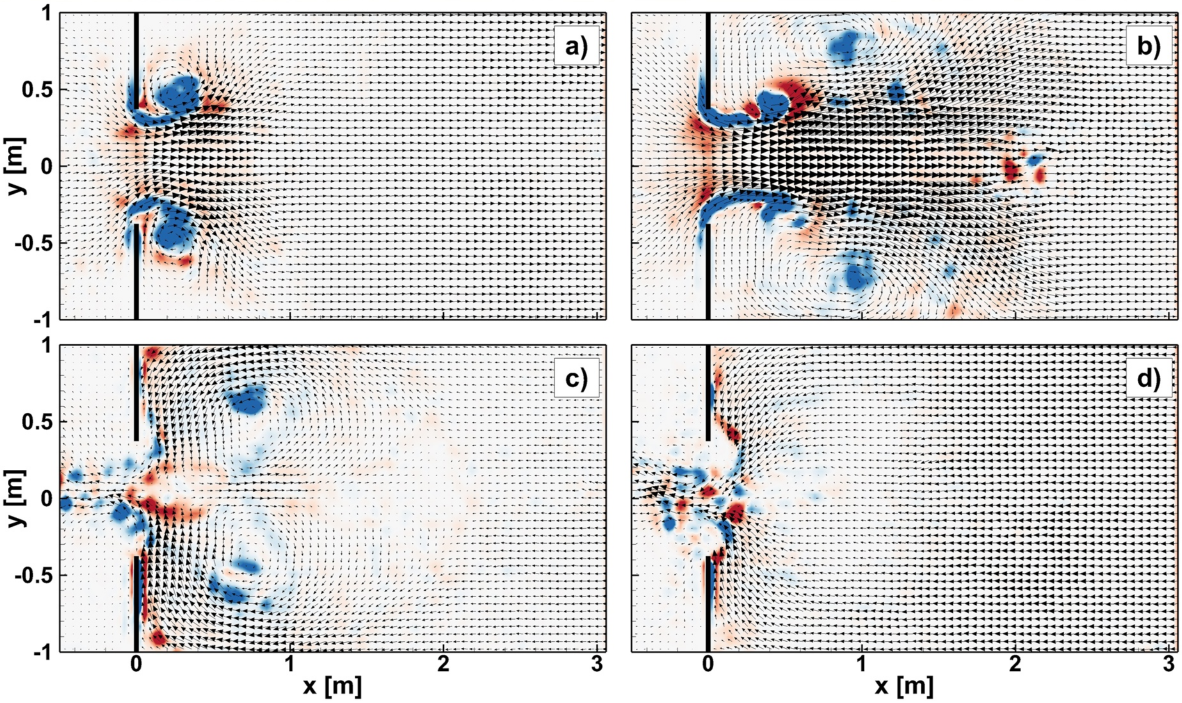

Figure 1. Top panel: Macrovortices generated by tidal currents in the western Sea of Okhotsk around the Shantar Islands and Uda Bay. Von Karman streets are observed during high tides with mean size of vortices of 500 m over a mean flow depth of 30 m. Adapted from the NASA image by Norman Kuring/NASA's Ocean Color Web, https://earthobservatory.nasa.gov/images/149148/tidal-vortices-in-the-sea-of-okhotsk. Four examples of measured 2D velocity fields for Experiment 04HR ($T = 100$ s, $\epsilon = 0.022$ and $L_g = 108.5$ m) together with the contours of the Okubo-Weiss parameter ($\lambda_0 = 1/4(S^2 - \omega^2)$) to help the identification of vortical structures. (a) rising flood; (b) falling flood; (c) beginning of ebb phase; (d) final stage of ebb phase.

Imposing the above similarity law helps in extending the results obtained in our laboratory experiments to real geophysical contexts. In fact, estuarine or semi-enclosed coastal bays are well described by the external parameters introduced by Toffolon et al. (2006) as shown in their figure 11, where several real estuaries have been classified in terms of friction parameter and convergence parameter using the semi-diurnal tide M_2 as the dominant tidal component. Provided the value of χ and γ and the geometrical scaling factors, see Supporting Information S1, the present results can be potentially transferred to the real world context.

For each experiment, we have collected 2D-velocity fields on the free surface using PIV with a high spatial and temporal resolution.

2.2. Filter-Space Technique for Nonlinear Energy and Enstrophy Transfers Estimation

We can safely define our problem as two dimensional, considering the large separation between the horizontal and vertical flow scales. For 2D flows, the two relevant global inviscid invariants are the kinetic energy $E_C = 1/2 < \mathbf{u} \cdot \mathbf{u} >$ and the enstrophy $Z = 1/2 < \boldsymbol{\omega} \cdot \boldsymbol{\omega} >$, where $\mathbf{u}$ is the velocity field and $\boldsymbol{\omega} = \nabla \times \boldsymbol{u}$ is the vorticity. To quantify the nonlinear energy and enstrophy fluxes in our experiments, we apply the FST. FST, differently from the more standard spectral methods, allows for computing the temporal and spatial distribution of the energy/enstrophy transfers in the domain. Moreover, FST can be applied to inhomogeneous flows without periodic boundary conditions and cases where FFT methods would require a preprocessing of the flow fields (domain periodizing, data tapering, and detrending), see for example, the discussion in Aluie et al. (2018) for the differences between FST and FFT methods.

FST is applied to the 2D-velocity measurements. This approach is based on building low-pass spectral filtered velocity fields by convolving the measured flow fields with a filter function with a kernel size (l). Thus, flow scales below l are suppressed and larger scales are retained. Varying the kernel size from the smallest length scale to the largest relevant scale of the flow produces a sequence of filtered fields at a prescribed l (Aluie et al., 2018; Eyink, 1995; Eyink & Aluie, 2009; Germano, 1992; Liao & Ouellette, 2013, 2014). For any field $\boldsymbol{f}(\boldsymbol{x})$, the low-pass filtered field is defined as $\overline{\boldsymbol{f}}_l(\boldsymbol{x}) = G_l * \boldsymbol{f}$, where $*$ stands for convolution and $G_l(\boldsymbol{x})$ is a normalized filtering function (e.g., a top-hat or Gaussian filter among others), typically characterized by a fast decay, with $\int G_l(\boldsymbol{x}) d^n\boldsymbol{x} = 1$ and l is the dimension of the kernel and n is the dimension of the space of integration.

Applying the filter to the Navier-Stokes equation and after some manipulations, we are left with the scale-filtered equation for the mean kinetic energy at the scale l, $E^{(l)}$, that can be written as (Liu et al., 1994; Rivera et al., 2014):

$$\frac{\partial E^{(l)}}{\partial t} + \frac{\partial T_i^{(l)}}{\partial x_i} = -\nu \frac{\partial u_i^{(l)}}{\partial x_j} \frac{\partial u_i^{(l)}}{\partial x_j} - \Pi^{(l)} - \alpha |\boldsymbol{u}^{(l)}|^2 \tag{1}$$

where $T_i^{(l)} = u_i^{(l)} \left(E^{(l)} + p^{(l)} \right) + u_j^{(l)} \tau_{ij}^{(l)}$ describes the transport terms that redistribute energy in space owing to the large-scale flow (first term), large-scale pressure (second term), and turbulence (third term). The second term is the energy dissipation, the term $\Pi^{(l)}$ is the new term arising from the application of the FST, and the last term represents the dissipation for large scale drag (α).

In particular, $\Pi^{(l)}$ is defined as:

$$\Pi^{(l)}(x, y, t) = -\tau_{ij}^{(l)}(x, y) S_{ij}^{(l)}(x, y) \tag{2}$$

where $\tau_{ij}^{(l)} = (u_i u_j)^{(l)} - u_i^{(l)} u_j^{(l)}$ is the residual stress tensor and $S_{ij}^{(l)} = 1/2 \left(\partial u_i^{(l)} / \partial x_j + \partial u_j^{(l)} / \partial x_i \right)$ is the filtered rate of strain (Eyink & Aluie, 2009; Liao & Ouellette, 2014). The term $\Pi^{(l)}$ represents the link between the filtered small scales (lower than l) and the resolved large flow scale (larger than l) as the source or sink of energy between the flow scales. It measures the spectral energy fluxes retaining the direction of the nonlinear transfer and, in particular, based on the sign convention assumed $\Pi^{(l)} > 0$ implies energy transfer to smaller scales and, conversely, $\Pi^{(l)} < 0$ denotes energy transfer toward larger scales.

Repeating the same operations on the enstrophy budget (Eyink, 1995), we can define a filtered enstrophy flux as:

$$Z^{(l)}(x, y, t) = -\sigma_i^{(l)}(x, y) \frac{\partial \omega^{(l)}(x, y)}{\partial x_i} \tag{3}$$

where $\sigma_i^{(l)} = (u_i\omega)^{(l)} - u_i^{(l)}\omega^{(l)}$ is the vorticity stress. Similar to $\Pi^{(l)}$, $Z^{(l)}$ measures the spectral enstrophy fluxes, with the same sign convention previously introduced.

The space and time average of $\Pi^{(l)}$ (Eyink, 2005) and $Z^{(l)}$ (Rivera et al., 2014) can be associated to the mean spectral fluxes in Fourier decomposition and, eventually, linked to power laws in the wavenumbers, such as the classical $-5/3$ Kolmogorov law for the direct energy cascade or the inverse energy cascade of the Kraichnan-Leith-Batchelor law (Alexakis & Biferale, 2018). We have provided the details of the computation of the scale-filtered fluxes in Supporting Information S1.

3. Results and Discussion

3.1. The Generation of Vortices at Several Scales

First, we discuss the Eulerian tidal flows generated in the experimental flume. Four snapshots of the two dimensional velocity fields of the Experiment 04HR ($T = 100$ s and $\epsilon = 0.022$) are shown in Figure 1. See the Movie S1 for the entire movie.

The contours represent the values of the Okubo-Weiss parameter λ_0 (Okubo, 1970; Weiss, 1991), see Supporting Information S1 for the details of the computation of the Okubo-Weiss parameter. Blue regions, corresponding to negative values of λ_0, denote the dominance of the local rotation (vortex), whereas red regions are dominated by strain. Panels (a) and (b) correspond to the flood phase and (c) and (d) to the ebb phase. The flow induced by the tidal wave of wavelength L_g (coming from the left in the figure) interacts with the tidal inlet, of size l_w, shedding vortices at a frequency much larger than that of the tidal period and with a typical size smaller than l_w, about $0.1–0.2l_w$. These vortices tend to merge and be deformed by the large scale shear flow, ultimately forming larger macro-vortices that, at the end of the flood, occupy the entire lateral tidal flats. These macro-vortices tend to be elongated in the longitudinal direction with a lateral dimension equal to $w_{ch}/2$ and greater than w_{ch} (or 2–3 times l_w) in the streamwise direction, see panel (b) of Figure 1.

Similar observations are reported in previous studies with simpler geometries, that is, rectangular channels (Nicolau del Roure et al., 2009; Vouriot et al., 2019). Different from previous studies, the flood macro-vortices are completely destroyed during the ebb phase, panels (c) and (d), leaving a flow substantially uniform along the entire channel width. The main reason for the different behavior can be ascribed to the channel geometry. In the present study, the presence of the later flats induces a more intense flow during the ebb, which is able to flush-out the main vortices.

During the ebb, small vortices are generated toward the open basin owing to a similar shedding mechanism from the tip of the tidal inlet. A similar process was observed in all experiments with the only difference relative to the final longitudinal extension of the flood macro-vortices, which increase inversely with the tidal period T, see Supporting Information S1 for the flow fields of all experiments. The generation of vortices as observed in our experiments qualitatively resembles the field observation as shown from the satellite image of figure 1 or figure 2 of Zhabin and Luk'yanova (2020).

The measured flow fields showed quite a distinct dynamics depending on the tidal phase. The flood is characterized by an intense vortex dynamics, including merging events and a tendency of the vortices to be deformed by the large scale shear flow. The vortices are surrounded by regions of intense strain (marked by positive values of the λ_0). On the contrary, the ebb phase is characterized by the annihilation of the macro-vortices owing to the large shear flow toward the open basin, with intense accelerations around the inlet.

The question that we shall address in this study is how the energy and enstrophy transfers are influenced by the different flow characteristics observed within a tidal period.

3.2. Nonlinear Energy and Enstrophy Transfers

We now analyze the nonlinear energy and enstrophy fluxes associated to the time periodic velocity fields, computing the spectral fluxes from Equations 2 and 3. Owing to the periodic nature of tidal flows, we subdivide a single cycle in six time frames on the basis of the dynamics observed from the velocity fields. The flood and ebb are analyzed in three sub-intervals $1/6T$ long, labeled in the following as Flood (Ebb) 1, 2 and 3.

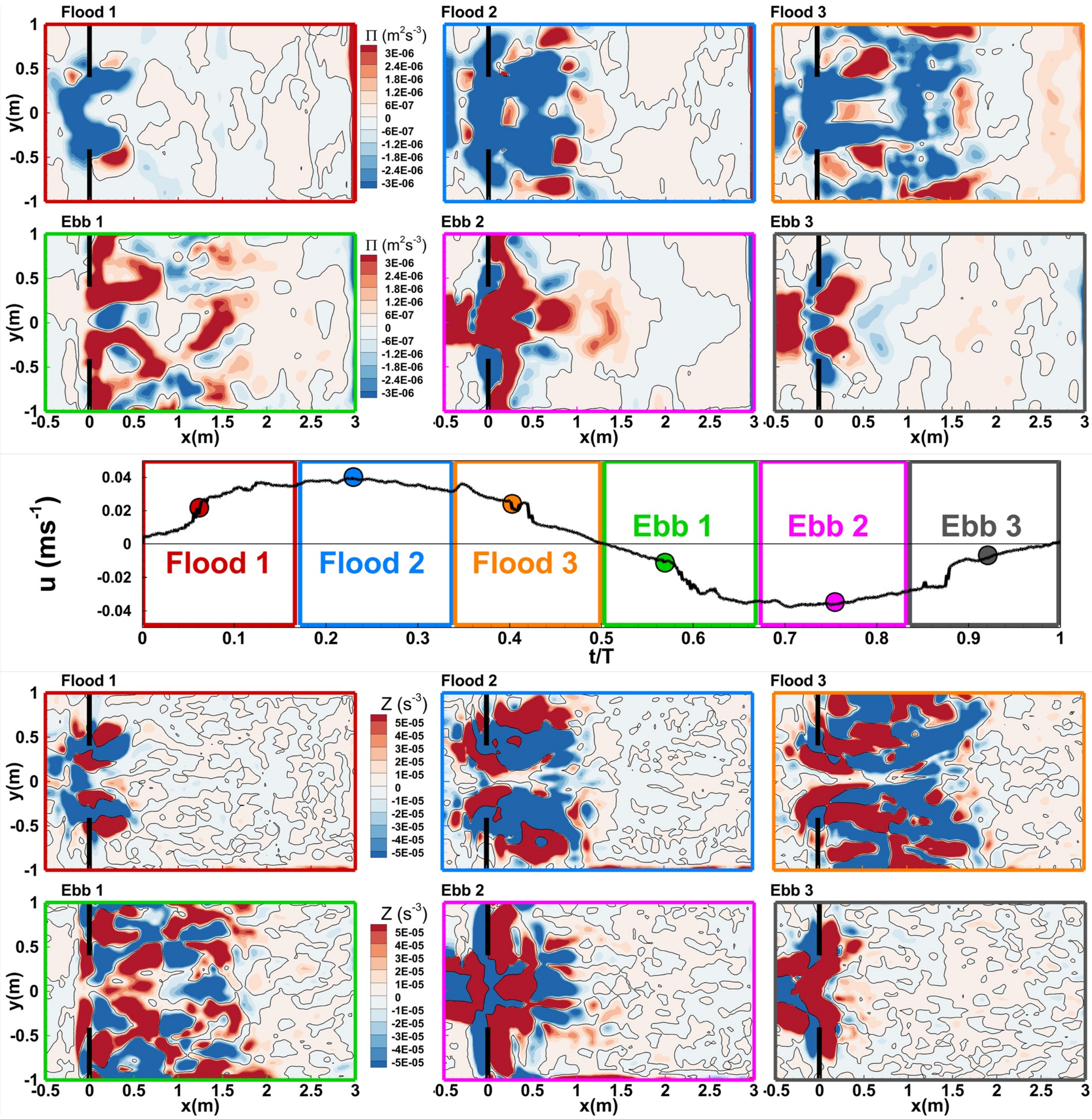

Figure 2. Contour maps of the spectral energy flux $\Pi^{(l)}$ (top six panels) and enstrophy flux $Z^{(l)}$ (bottom six panels) computed for a filter scale $l = 0.15 l_w$ ($l_w = 0.86$ m) at different tidal phases for Experiment 01HR ($T = 180$ s, $\epsilon = 0.0325$ and $L_g = 195.3$ m). The central panel reports a time signal of the measured velocity at the inlet and it is used to identify the six sub-intervals. The dots correspond to the exact times where the $\Pi^{(l)}$ and $Z^{(l)}$ maps are taken.

Examples of spatial distributions of the ensemble averaged spectral energy flux $\Pi^{(l)}$ and enstrophy flux $Z^{(l)}$ for a selected scale $l = 0.15 l_w$ are shown in Figure 2 for six instants in a tidal period. The maps represent a single instant in the period, marked by colored dots in the middle panel of Figure 2, where the time signal of the velocity in front of the inlet is reported to help the identification of the tidal phase. The spatial maps of both of $\Pi^{(l)}$ and $Z^{(l)}$ reveal some common features between the fluxes of the two invariants (energy and enstrophy). In particular, a marked spatial inhomogeneity is revealed. In fact, the most active area is limited to the portion of the domain around the tidal inlet up to a distance of about $\sim 3 l_w$ during the flood. Moreover, it is interesting to note how the fluxes maintain a time dependence, which is the consequence of a periodic forcing. In particular, the flood is characterized by the presence of a larger and larger portion of the domain where $\Pi^{(l)} < 0$ in a background field of small values of $\Pi^{(l)}$, that is, the energy is gained by scales larger than l. The opposite is observed during the ebb when $\Pi^{(l)}$ reverses its sign, becoming highly positive, implying a transfer toward scales smaller than l. The fluxes of $Z^{(l)}$ show a different evolution especially for the distribution of the positive and negative areas with the highest values around the inlet as the energy fluxes. Increasing the kernel l leads to smoother fields of the spectral fluxes, as expected from the FST method. Examples of maps of $\Pi^{(l)}$ and $Z^{(l)}$ for $l = l_w$ and $l = 2l_w$ are reported in Supporting Information S1.

To better highlight the transient nature of energy and enstrophy transfers, we report in Figure 3 the spatial-averaged values of the fluxes $\langle \Pi \rangle$ (panels a–d) and $\langle Z \rangle$ (panels e–h) as a function of the dimensionless time t/T and filter scales l/l_w for all the experiments.

This is probably the most important result of the present analysis and it is the first evidence of the periodic dependence of the spectral fluxes. The time maps emphasize the differences between the flood and ebb phases for both fluxes. During the flood, flow scales in the range $0.15 \lesssim l/l_w \lesssim 2.5$ are characterized by a transfer of energy toward the larger scales (inverse energy cascade), whereas scales above $l/l_w \gtrsim 2.5$ tend to invert their sign and, therefore, transfer direction, leading to a direct energy cascade. The ebb phase is almost perfectly mirrored with respect to the flood. It is interesting to note that, during flood, length scales below the value of 0.15 show positive values of $\langle \Pi \rangle$, although not particularly intense. We will comment further on this later on. Enstrophy shows a similar behavior in terms of periodicity, although the sign remains fairly constant along the scales. The flood seems to be dominated by an inverse cascade of enstrophy and ebb, by a direct cascade of enstrophy. The most relevant change of sign from positive to negative is observed for $l/l_w \lesssim 0.15$ during most of the flood phase.

Decreasing the tidal period, from panels (a) to (d), tends to make the separation of the flow scales more evident and sharper, for example, two positive maxima clearly appear in Experiment 04HR ($T = 100$ s) (panel d). Cascade transitions that cause a change in the direction of the energy transfers are found in turbulent flow systems, when the controlling parameters are varied, for example, turbulence in layers of finite thickness (Celani et al., 2010) or in rotating systems (Buzzicotti et al., 2018). Several possible scenarios can be foreseen (Alexakis & Biferale, 2018) and, among them, the system can transit from a forward cascade to a split cascade as found for thin layers or rotating turbulence. The results indicate that tidal flows undergo a similar scenario during a single period. The more intense fluxes observed for a decreasing tidal period (and tidal wave length) could be due to the increase in the velocity intensities.

In natural estuaries or coastal bays, the results of Figure 3 suggest that, for a given period of the dominant tide, shallower flow conditions (i.e., for decreasing mean flow depth D_0) enhance the establishment of higher energy and enstrophy fluxes with a more marked transition between the flow scales and the tidal phases.

Further reducing the dimensions of the problem by averaging over time, the energy and enstrophy fluxes only depend on l/l_w. We indicated the space-time averaged quantities as $\langle\langle \Pi \rangle\rangle$ and $\langle\langle Z \rangle\rangle$. Averaging over the entire time of the process is common in order to grasp the overall picture of the energy/enstrophy transfers and the link to the spectral cascades (Aluie et al., 2018; Benavides & Alexakis, 2017; Fang et al., 2019; Fang & Ouellette, 2016; Liao & Ouellette, 2013, 2014, 2015a, 2015b; Rivera et al., 2014). Care must be taken in the present case since our process is periodic, contrary to most of the cited studies that dealt with statistically steady flows. We perform time averages over different time intervals and in particular, over the flood and ebb phases separately and over the entire period T.

The results of the different time averages are summarized in Figure 4. Panels (a) and (b) show the fluxes $\langle\langle \Pi \rangle\rangle$ and $\langle\langle Z \rangle\rangle$ for all experiments dividing the flood phase from the ebb. As explained in detail in Supporting Information S1, the error bars reported in the plots refer to the RMSD computed among the different realizations. RMSD is about 8% of the mean values for a scale below 2.5 and tend to increase for a larger scale up to a value of about 15%.

Two fundamental characteristics of the process are evident. First, the mean spectral energy flux changes the sign at two specific length scales. In particular, during the flood, $\langle\langle \Pi \rangle\rangle$ is positive for scales lower than $l/l_w \lesssim 0.15$ and then becomes strongly negative in the range $0.15 \lesssim l/l_w \lesssim$ 2–2.5. The first zero-crossing is independent of the forcing tidal period, whereas the second depends on the tidal period. Larger flow scales ($l/l_w \gtrsim 2.5$) are

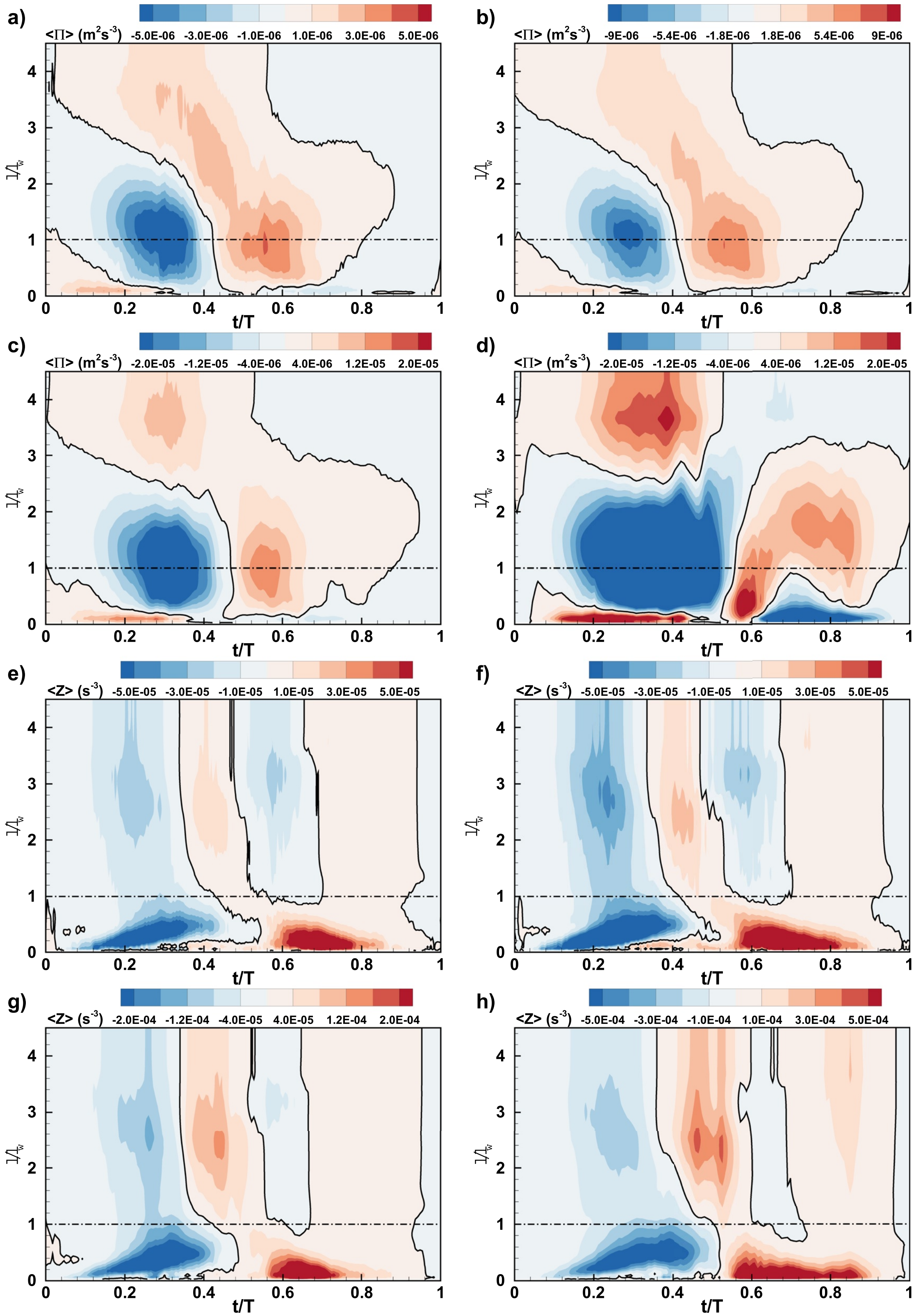

Figure 3. Contour maps of the space averaged $\langle \Pi \rangle$ and $\langle Z \rangle$ as a function of nondimensional tidal phase t/T and nondimensional scale l/l_w. Panels (a–d) represent $\langle \Pi \rangle$ of Experiment 01HR ($T = 180$ s, $\epsilon = 0.0325$ and $L_g = 195.3$ m), 02HR ($T = 160$ s, $\epsilon = 0.0308$ and $L_g = 173.6$ m), 03HR ($T = 130$ s, $\epsilon = 0.0225$ and $L_g = 141.0$ m) and 04HR ($T = 100$ s, $\epsilon = 0.0217$ and $L_g = 108.5$ m), respectively. Panels (e–h) represent $\langle Z \rangle$ of Experiment 01HR ($T = 180$ s, $\epsilon = 0.0325$ and $L_g = 195.3$ m), 02HR ($T = 160$ s, $\epsilon = 0.0308$ and $L_g = 173.6$ m), 03HR ($T = 130$ s, $\epsilon = 0.0225$ and $L_g = 141.0$ m) and 04HR ($T = 100$ s, $\epsilon = 0.0217$ and $L_g = 108.5$ m), respectively.

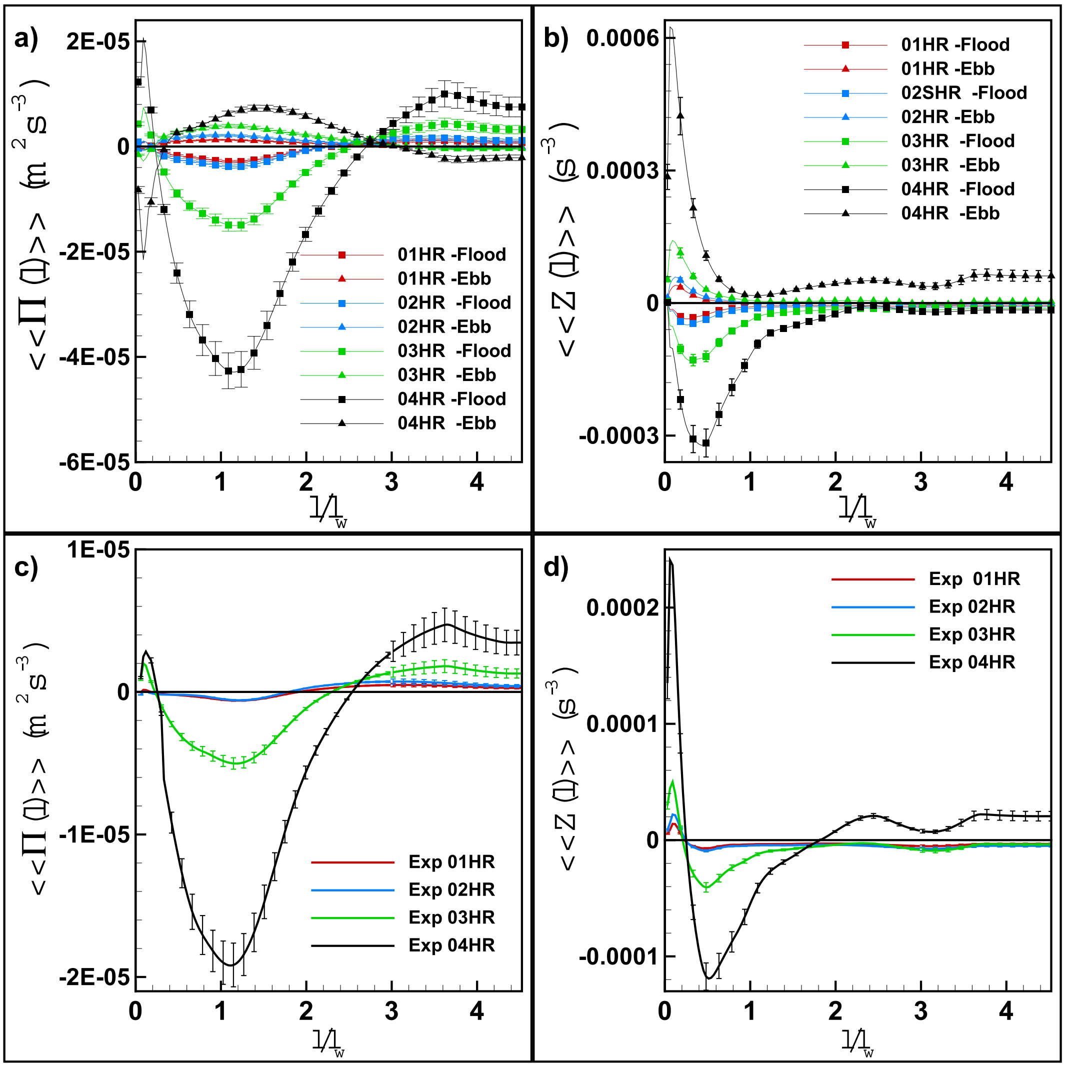

Figure 4. Temporal and spatial average of Π and Z as a function of the nondimensional scale l/l_w. Panel (a) $\langle\langle\Pi\rangle\rangle$ and panel (b) $\langle\langle Z\rangle\rangle$ for all experiments averaged on the flood and ebb phases. Panel (c) $\langle\langle\Pi\rangle\rangle$ and panel (d) $\langle\langle Z\rangle\rangle$ for all experiments averaged on tidal period.

characterized by positive fluxes. Second, the energy fluxes during the two phases show a symmetry with respect to the fixed zero-crossing scales. However, the energy fluxes at the large scale during the ebb are much less vigorous compared to the more energetic flood phase. Similarly, enstrophy changes the direction of transfer according to the tidal phase. The flood is dominated by a negative flux, whereas the ebb is characterized by positive fluxes.

We now attempt to provide a physical description of the processes behind the behavior of the fluxes discussed so far. First, it is important to acknowledge a limitation of the present analysis that is somehow related to the application of FST and the scale resolved by the LS-PIV measurements. In particular, it is not possible to cover the entire range of scales involved in the process. In the small scale range, we do not resolve the viscous scales where energy dissipation occurs owing to viscous effects. Viscosity would act at the Kolmogorov scale that can be evaluated as $\eta \sim L/R_e^{3/4}$ (Tennekes et al., 1972). In present experiments, η assumes a value of about 10^{-4}m, too small for the LSP-IV resolution that is about 2 cm. However, as expected, the energy is transferred to the smaller scale in *weak* direct energy cascade fashion for $l/l_w \lesssim 0.15$ and we observe that the fluxes tend to be zero for $l/l_w \to 0$. Second, we are not able to describe the largest scale (channel length), where a large scale quadratic dissipation proportional to the drag α occurs, see the last term in Equation 1. This is limited by the FST computation that does not allow to reach those scales. Again, we may expect that the fluxes tend to be zero for the largest scales and the measurements seem to be consistent with this.

From a physical standpoint, both energy and enstrophy fluxes are controlled by a delicate balance between stress and strain, the former, and vorticity stress and vorticity gradient, the latter. The relative alignments among these quantities are even more important than their intensities (Liao & Ouellette, 2014; Xiao et al., 2009). Previous studies dedicated to the physical explanation of energy and enstrophy cascades showed how vortex merging (Aluie & Kurien, 2011; Kraichnan, 1967) and thinning (Chen et al., 2006; Kraichnan, 1976; Xiao et al., 2009) are responsible for an inverse energy cascade, whereas strain dominated flow regions are mostly responsible for a direct cascade (Chen et al., 2003). These conclusions were often drawn by computing the Okubo-Weiss parameter and conditionally averaging the fluxes with the values of λ_0.

In the present case, we observed that the flow fields during the flood phase is, on average, dominated by negative values of λ_0 indicating the presence of vortical structures that are strongly influenced by the mean large scale advection, causing merging and, more importantly, thinning processes. Chen et al. (2006) provided a clear physical picture on the process that modifies a vortex immersed in a large-scale strain field (the large scale tidal flow in the present case). A small scale vortex is elongated along its stretching direction and thinned along its compressing direction, reducing the velocity and energy around it as imposed by Kelvin's theorem. At the same time, the velocity will change its alignment, producing a net positive or tensile stress along the stretching axis, ultimately increasing the large scale energy. The associated $\ll\Pi\gg$ tends to be negative in the range of scale where these processes are active and positive for the larger scales where strain tends to dominate. Enstrophy is also influenced by the rotation dominated scales and tends to be negative as the energy fluxes, whereas it tends to vanish for larger scales.

When the flow reverses during the ebb phase, the flow is mostly dominated by large-scale strain and λ_0 is mostly positive. In this case, the vorticity stress of Equation 3 tends to be antiparallel to the large-scale vorticity gradient, producing, on average, a direct cascade of enstrophy (Chen et al., 2003). Simultaneously, the energy fluxes are mostly positive owing to a changing in the alignment of the small scale turbulent stresses and the large scale strain. In particular, it is reasonable to assume that the stresses tend to be more orthogonal to the strain field (Liao & Ouellette, 2014; Xiao et al., 2009), as typical of open channel shear flows (Enrile et al., 2020; Nikora et al., 2007; Stocchino et al., 2011), and thus the fluxes tend to be positive as a signature of a direct energy cascade.

The period-averaged energy/enstrophy transfer process is shown in Figures 4c and 4d, where we report the tidal period averaged fluxes. The overall process seems to be dominated by a split-energy cascade where the large scale flow gains energy from the smaller scales in a range $0.15 \lesssim l/l_w \lesssim 2$–$2.5$ and loses energy in favor to the small scales for larger separations and for $l/l_w \lesssim 0.15$, where viscous dissipation ultimately occurs. A similar behavior has been described in a turbulence-like flows study characterized by the co-existence of 2D flow structures at different scales (Aluie & Kurien, 2011; Benavides & Alexakis, 2017).

The energy cascade transitions found in the present study could be linked to physical length scales relevant in natural contexts. In fact, the simplified geometry represented in our experiments is commonly found in coastal semi-enclosed embankments or bays or even in estuarine regions. The presence of a barrier island or similar coastal features are known to influence the local dynamics and transport properties (Blondeaux & Vittori, 2020; Nicolau del Roure et al., 2009; Vouriot et al., 2019). The present results suggest that the lateral extension of the barrier island is a crucial length of the energy process. In fact, for flow scales up to few times the latter length scale (l_w in the present case), the flow should be dominated by a negative energy flux, whereas larger flow scales are dominated by direct energy cascades. Moreover, the presence of a multiple cascade could also influence the mixing properties. In fact, it is a well-known link between the energy cascades and the dispersion properties, see LaCasce (2008) for a review on the topic. The change in sign of the fluxes should be recovered also in a change of regime from the dispersion standpoint, that is, from a local dynamics, the mixing is governed by small scale flow structures, to a nonlocal dynamics, where the mixing is governed by large scale flow structures. This is an important aspect to be considered when transport processes are analyzed in realistic coastal areas dominated by the tides especially in shallow water conditions.

4. Conclusions

This study explored the challenging description of the exchange of energy and enstrophy among the range of scales of an extremely common class of coastal flows, that is, tidal currents. We approached the problem focusing the attention on the interaction of a tidal flow with an inlet using a large-scale laboratory model. In this controlled environment, we recreated the commonly observed vortex shedding and merging that are expected to play a major role in the energy transfers. We preferred a FST rather the more standard spectral approach owing to the wealth of information that this framework offers. The results undoubtedly showed the transitional character of the energy/enstrophy transfers during a single tidal period and the coexistence of multiple cascades. In fact, inverse energy and split-energy cascades were found to be the dominant processes. The pathways of energy toward the large scale were linked to vortex merging and thinning observed during floods, whereas a direct cascade was observed during the ebb when the mean flow caused the rapid decay of the tidal channel vortical structures and the large-scale strain dominates. Two length scales appeared to dominate the process, the dimension of the tidal inlet that controls the small scale vortex shedding and the width of the tidal flats that is related to the size of the largest macro-vortices. The existence of multiple cascades could be a challenging process to be reproduced using coastal circulation models based on the RANS equations. In fact, the inverse energy cascade is often associated to the *negative eddy viscosity* process and this implies that standard modeling approaches based on the eddy viscosity closure should be able to reproduce negative values of the momentum transport coefficient in order to correctly describe a negative energy flux.

Our results contributed to the developing literature on the description of energy budget in geophysical flows and represent one of the few examples of application of filtering techniques to coastal environments.

Conflict of Interest

The authors declare no conflicts of interest relevant to this study.

Data Availability Statement

Data Management Repository available at doi: https://doi.org/10.5281/zenodo.5898588.

Acknowledgments
This research has not been supported by external funding. The authors want to thank Professor A. Mazzino for his helpful comments during the preliminary stage of this study.

References

Alexakis, A., & Biferale, L. (2018). Cascades and transitions in turbulent flows. *Physics Reports*, *767*, 1–101. https://doi.org/10.1016/j.physrep.2018.08.001

Aluie, H. (2011). Compressible turbulence: The cascade and its locality. *Physical Review Letters*, *106*(17), 174502. https://doi.org/10.1103/physrevlett.106.174502

Aluie, H., & Eyink, G. L. (2009). Localness of energy cascade in hydrodynamic turbulence. II. Sharp spectral filter. *Physics of Fluids*, *21*(11), 115108. https://doi.org/10.1063/1.3266948

Aluie, H., & Eyink, G. L. (2010). Scale locality of magnetohydrodynamic turbulence. *Physical Review Letters*, *104*(8), 081101. https://doi.org/10.1103/physrevlett.104.081101

Aluie, H., Hecht, M., & Vallis, G. K. (2018). Mapping the energy cascade in the North Atlantic Ocean: The coarse-graining approach. *Journal of Physical Oceanography*, *48*(2), 225–244. https://doi.org/10.1175/jpo-d-17-0100.1

Aluie, H., & Kurien, S. (2011). Joint downscale fluxes of energy and potential enstrophy in rotating stratified Boussinesq flows. *EPL (Europhysics Letters)*, *96*(4), 44006. https://doi.org/10.1209/0295-5075/96/44006

Benavides, S. J., & Alexakis, A. (2017). Critical transitions in thin layer turbulence. *Journal of Fluid Mechanics*, *822*, 364–385. https://doi.org/10.1017/jfm.2017.293

Blondeaux, P., & Vittori, G. (2020). Modeling transverse coastal bedforms at Anna Maria Island (Florida). *Journal of Geophysical Research: Oceans*, *125*(7), e2019JC015837. https://doi.org/10.1029/2019jc015837

Buzzicotti, M., Aluie, H., Biferale, L., & Linkmann, M. (2018). Energy transfer in turbulence under rotation. *Physical Review Fluids*, *3*(3), 034802. https://doi.org/10.1103/physrevfluids.3.034802

Cai, H., Savenije, H. H., & Toffolon, M. (2012). A new analytical framework for assessing the effect of sea-level rise and dredging on tidal damping in estuaries. *Journal of Geophysical Research*, *117*(C9). https://doi.org/10.1029/2012jc008000

Celani, A., Musacchio, S., & Vincenzi, D. (2010). Turbulence in more than two and less than three dimensions. *Physical Review Letters*, *104*(18), 184506. https://doi.org/10.1103/physrevlett.104.184506

Chen, S., Ecke, R. E., Eyink, G. L., Rivera, M., Wan, M., & Xiao, Z. (2006). Physical mechanism of the two-dimensional inverse energy cascade. *Physical Review Letters*, *96*(8), 084502. https://doi.org/10.1103/physrevlett.96.084502

Chen, S., Ecke, R. E., Eyink, G. L., Wang, X., & Xiao, Z. (2003). Physical mechanism of the two-dimensional enstrophy cascade. *Physical Review Letters*, *91*(21), 214501. https://doi.org/10.1103/physrevlett.91.214501

Enrile, F., Besio, G., & Stocchino, A. (2020). Eulerian spectrum of finite-time Lyapunov exponents in compound channels. *Meccanica*, *55*(9), 1821–1828. https://doi.org/10.1007/s11012-020-01217-y

Enrile, F., Besio, G., Stocchino, A., Magaldi, M., Mantovani, C., Cosoli, S., et al. (2018). Evaluation of surface Lagrangian transport barriers in the Gulf of Trieste. *Continental Shelf Research*, *167*, 125–138. https://doi.org/10.1016/j.csr.2018.04.016

Enrile, F., Besio, G., Stocchino, A., & Magaldi, M. G. (2019). Influence of initial conditions on absolute and relative dispersion in semi-enclosed basins. *PLoS One*, *14*(7), e0217073. https://doi.org/10.1371/journal.pone.0217073

Eyink, G. L. (1995). Exact results on scaling exponents in the 2D enstrophy cascade. *Physical Review Letters*, *74*(19), 3800–3803. https://doi.org/10.1103/physrevlett.74.3800

Eyink, G. L. (2005). Locality of turbulent cascades. *Physica D: Nonlinear Phenomena*, *207*(1–2), 91–116. https://doi.org/10.1016/j.physd.2005.05.018

Eyink, G. L., & Aluie, H. (2009). Localness of energy cascade in hydrodynamic turbulence. I. Smooth coarse graining. *Physics of Fluids*, *21*(11), 115107. https://doi.org/10.1063/1.3266883

Fang, L., Balasuriya, S., & Ouellette, N. T. (2019). Local linearity, coherent structures, and scale-to-scale coupling in turbulent flow. *Physical Review Fluids*, *4*(1), 014501. https://doi.org/10.1103/physrevfluids.4.014501

Fang, L., & Ouellette, N. T. (2016). Advection and the efficiency of spectral energy transfer in two-dimensional turbulence. *Physical Review Letters*, *117*(10), 104501. https://doi.org/10.1103/physrevlett.117.104501

Germano, M. (1992). Turbulence: The filtering approach. *Journal of Fluid Mechanics*, *238*, 325–336. https://doi.org/10.1017/s0022112092001733

Geyer, W. R., & MacCready, P. (2014). The estuarine circulation. *Annual Review of Fluid Mechanics*, *46*(1), 175–197. https://doi.org/10.1146/annurev-fluid-010313-141302

Kelly, S. M., Nash, J. D., Martini, K. I., Alford, M. H., & Kunze, E. (2012). The cascade of tidal energy from low to high modes on a continental slope. *Journal of Physical Oceanography*, *42*(7), 1217–1232. https://doi.org/10.1175/jpo-d-11-0231.1

Khatri, H., Sukhatme, J., Kumar, A., & Verma, M. K. (2018). Surface ocean enstrophy, kinetic energy fluxes, and spectra from satellite altimetry. *Journal of Geophysical Research: Oceans*, *123*(5), 3875–3892. https://doi.org/10.1029/2017jc013516

Kolmogorov, A. N. (1941). The local structure of turbulence in incompressible viscous fluid for very large Reynolds numbers. *Comptes Rendus de l'Académie des Sciences URSS*, *30*, 301–305.

Kraichnan, R. H. (1967). Inertial ranges in two-dimensional turbulence. *The Physics of Fluids*, *10*(7), 1417–1423. https://doi.org/10.1063/1.1762301

Kraichnan, R. H. (1976). Eddy viscosity in two and three dimensions. *Journal of the Atmospheric Sciences*, *33*(8), 1521–1536. https://doi.org/10.1175/1520-0469(1976)033<1521:evitat>2.0.co;2

LaCasce, J. (2008). Statistics from Lagrangian observations. *Progress in Oceanography*, *77*(1), 129–29. https://doi.org/10.1016/j.pocean.2008.02.002

Liao, Y., & Ouellette, N. T. (2013). Spatial structure of spectral transport in two-dimensional flow. *Journal of Fluid Mechanics*, *725*, 281–298. https://doi.org/10.1017/jfm.2013.187

Liao, Y., & Ouellette, N. T. (2014). Geometry of scale-to-scale energy and enstrophy transport in two-dimensional flow. *Physics of Fluids*, *26*(4), 045103. https://doi.org/10.1063/1.4871107

Liao, Y., & Ouellette, N. T. (2015). Correlations between the instantaneous velocity gradient and the evolution of scale-to-scale fluxes in two-dimensional flow. *Physical Review E*, *92*(3), 033017. https://doi.org/10.1103/physreve.92.033017

Liao, Y., & Ouellette, N. T. (2015). Long-range ordering of turbulent stresses in two-dimensional flow. *Physical Review E*, *91*(6), 063004. https://doi.org/10.1103/physreve.91.063004

Liu, S., Meneveau, C., & Katz, J. (1994). On the properties of similarity subgrid-scale models as deduced from measurements in a turbulent jet. *Journal of Fluid Mechanics*, *275*, 83–119. https://doi.org/10.1017/s0022112094002296

MacCready, P., & Geyer, W. R. (2010). Advances in estuarine physics. *Annual Review of Marine Science*, *2*(1), 35–58. https://doi.org/10.1146/annurev-marine-120308-081015

Nicolau del Roure, F., Socolofsky, S. A., & Chang, K.-A. (2009). Structure and evolution of tidal starting jet vortices at idealized barotropic inlets. *Journal of Geophysical Research*, *114*(C5), C05024. https://doi.org/10.1029/2008jc004997

Nikora, V., Nokes, R., Veale, W., Davidson, M., & Jirka, G. (2007). Large-scale turbulent structure of uniform shallow free-surface flows. *Environmental Fluid Mechanics*, *7*(2), 159–172. https://doi.org/10.1007/s10652-007-9021-z

Okubo, A. (1970). Horizontal dispersion of floatable particles in the vicinity of velocity singularities such as convergences. *Deep Sea Research and Oceanographic Abstracts*, *17*(3), 445–454. https://doi.org/10.1016/0011-7471(70)90059-8

Poje, A. C., Özgökmen, T. M., Bogucki, D. J., & Kirwan, A. (2017). Evidence of a forward energy cascade and Kolmogorov self-similarity in submesoscale ocean surface drifter observations. *Physics of Fluids*, *29*(2), 020701. https://doi.org/10.1063/1.4974331

Rivera, M., Aluie, H., & Ecke, R. (2014). The direct enstrophy cascade of two-dimensional soap film flows. *Physics of Fluids*, *26*(5), 055105. https://doi.org/10.1063/1.4873579

Savage, A. C., Arbic, B. K., Richman, J. G., Shriver, J. F., Alford, M. H., Buijsman, M. C., et al. (2017). Frequency content of sea surface height variability from internal gravity waves to mesoscale eddies. *Journal of Geophysical Research: Oceans*, *122*(3), 2519–2538. https://doi.org/10.1002/2016jc012331

Scott, R. B., & Wang, F. (2005). Direct evidence of an oceanic inverse kinetic energy cascade from satellite altimetry. *Journal of Physical Oceanography*, *35*(9), 1650–1666. https://doi.org/10.1175/jpo2771.1

Siegelman, L., Klein, P., Ingersoll, A. P., Ewald, S. P., Young, W. R., Bracco, A., et al. (2022). Moist convection drives an upscale energy transfer at Jovian high latitudes. *Nature Physics*, 1–5. https://doi.org/10.1038/s41567-021-01458-y

Stocchino, A., Besio, G., Angiolani, S., & Brocchini, M. (2011). Lagrangian mixing in straight compound channels. *Journal of Fluid Mechanics*, *675*, 168–198. https://doi.org/10.1017/s0022112011000127

Suara, K., Chanson, H., Borgas, M., & Brown, R. J. (2017). Relative dispersion of clustered drifters in a small micro-tidal estuary. *Estuarine, Coastal and Shelf Science*, *194*, 1–15. https://doi.org/10.1016/j.ecss.2017.05.001

Tennekes, H., Lumley, J. L., & Lumley, J. L. (1972). *A first course in turbulence*. MIT press.

Thiesset, F., & Danaila, L. (2020). The illusion of a Kolmogorov cascade. *Journal of Fluid Mechanics*, *902*. https://doi.org/10.1017/jfm.2020.594

Toffolon, M., Vignoli, G., & Tubino, M. (2006). Relevant parameters and finite amplitude effects in estuarine hydrodynamics. *Journal of Geophysical Research*, *111*(C10), C10014. https://doi.org/10.1029/2005jc003104

Torres, H. S., Klein, P., Menemenlis, D., Qiu, B., Su, Z., Wang, J., et al. (2018). Partitioning ocean motions into balanced motions and internal gravity waves: A modeling study in anticipation of future space missions. *Journal of Geophysical Research: Oceans*, *123*(11), 8084–8105. https://doi.org/10.1029/2018jc014438

Valle-Levinson, A. (2010). *Contemporary issues in estuarine physics*. Cambridge University Press.

Vouriot, C. V., Angeloudis, A., Kramer, S. C., & Piggott, M. D. (2019). Fate of large-scale vortices in idealized tidal lagoons. *Environmental Fluid Mechanics*, *19*(2), 329–348. https://doi.org/10.1007/s10652-018-9626-4

Weiss, J. (1991). The dynamics of enstrophy transfer in two-dimensional hydrodynamics. *Physica D*, *48*(2–3), 272–294. https://doi.org/10.1016/0167-2789(91)90088-q

Whilden, K. A., Socolofsky, S. A., Chang, K.-A., & Irish, J. L. (2014). Using surface drifter observations to measure tidal vortices and relative diffusion at Aransas pass, Texas. *Environmental Fluid Mechanics*, *14*(5), 1147–1172. https://doi.org/10.1007/s10652-014-9361-4

Xiao, Z., Wan, M., Chen, S., & Eyink, G. (2009). Physical mechanism of the inverse energy cascade of two-dimensional turbulence: A numerical investigation. *Journal of Fluid Mechanics*, *619*, 1–44. https://doi.org/10.1017/s0022112008004266

Zhabin, I., & Luk'yanova, N. (2020). Sub-Mesoscale Vortex Streets in the Region of the Shantar Islands (Sea of Okhotsk), According to Satellite Remote Sensing Data. *Izvestiya, Atmospheric and Oceanic Physics*, *56*(12), 1615–1620. https://doi.org/10.1134/s0001433820120609

References From the Supporting Information

Aluie, H., Hecht, M., & Vallis, G. K. (2018). Mapping the energy cascade in the North Atlantic Ocean: The coarse-graining approach. *Journal of Physical Oceanography*, *48*(2), 225–244. https://doi.org/10.1175/jpo-d-17-0100.1

Okubo, A. (1970). Horizontal dispersion of floatable particles in the vicinity of velocity singularities such as convergences. *Deep Sea Research and Oceanographic Abstracts*, *17*(3), 445–454. https://doi.org/10.1016/0011-7471(70)90059-8

Rivera, M., Aluie, H., & Ecke, R. (2014). The direct enstrophy cascade of two-dimensional soap film flows. *Physics of Fluids*, *26*(5), 055105. https://doi.org/10.1063/1.4873579

Toffolon, M., Vignoli, G., & Tubino, M. (2006). Relevant parameters and finite amplitude effects in estuarine hydrodynamics. *Journal of Geophysical Research*, *111*(C10), C10014. https://doi.org/10.1029/2005jc003104

Weiss, J. (1991). The dynamics of enstrophy transfer in two-dimensional hydrodynamics. *Physica D*, *48*(2–3), 272–294. https://doi.org/10.1016/0167-2789(91)90088-q